

Astrometry of H₂O Masers in Nearby Star-Forming Regions with VERA. III. IRAS 22198+6336 in L1204G

Tomoya HIROTA,^{1,2} Kazuma ANDO,³ Takeshi BUSHIMATA,^{1,4} Yoon Kyung CHOI,¹
Mareki HONMA,^{1,2} Hiroshi IMAI,⁵ Kenzaburo IWADATE,⁶ Takaaki JIKE,⁶
Seiji KAMENO,⁵ Osamu KAMEYA,^{2,6} Ryuichi KAMOHARA,¹ Yukitoshi KAN-YA,⁷
Noriyuki KAWAGUCHI,^{1,2,4} Masachika KIJIMA,² Mi Kyoung KIM,^{1,8} Hideyuki KOBAYASHI,^{1,4,6,8}
Seisuke KUJI,⁶ Tomoharu KURAYAMA,⁹ Seiji MANABE,^{2,6} Makoto MATSUI,³
Naoko MATSUMOTO,² Takeshi MIYAJI,^{1,4} Atsushi MIYAZAKI,⁶ Takumi NAGAYAMA,³
Akiharu NAKAGAWA,⁵ Daichi NAMIKAWA,³ Daisuke NYU,³ Chung Sik OH,^{1,8}
Toshihiro OMODAKA,⁵ Tomoaki OYAMA,¹ Satoshi SAKAI,⁶ Tetsuo SASAO,^{9,10}
Katsuhisa SATO,⁶ Mayumi SATO,^{1,8} Katsunori M. SHIBATA,^{1,2,4} Yoshiaki TAMURA,^{2,6}
Kosuke UEDA,³ and Kazuyoshi YAMASHITA²

¹*Mizusawa VERA Observatory, National Astronomical Observatory of Japan,
2-21-1 Osawa, Mitaka, Tokyo 181-8588*

²*Department of Astronomical Sciences, Graduate University for Advanced Studies,
2-21-1 Osawa, Mitaka, Tokyo 181-8588*

³*Graduate School of Science and Engineering, Kagoshima University,
1-21-35 Korimoto, Kagoshima, Kagoshima 890-0065*

⁴*Space VLBI Project, National Astronomical Observatory of Japan,
2-21-1 Osawa, Mitaka, Tokyo 181-8588*

⁵*Faculty of Science, Kagoshima University,
1-21-35 Korimoto, Kagoshima, Kagoshima 890-0065*

⁶*Mizusawa VERA Observatory, National Astronomical Observatory of Japan,
2-12 Hoshi-ga-oka, Mizusawa-ku, Oshu-shi, Iwate 023-0861*

⁷*Department of Astronomy, Yonsei University,
134 Shinchong-dong, Seodaemun-gu, Seoul 120-749, Republic of Korea*

⁸*Department of Astronomy, Graduate School of Science, The University of Tokyo,
7-3-1 Hongo, Bunkyo-ku, Tokyo 113-0033*

⁹*Korean VLBI Network, Korea Astronomy and Space Science Institute,
P.O.Box 88, Yonsei University, 134 Shinchon-dong, Seodaemun-gu, Seoul 120-749, Republic of Korea*

¹⁰*Department of Space Survey and Information Technology, Ajou University,
Suwon 443-749, Republic of Korea
tomoya.hirota@nao.ac.jp*

(Received 2008 April 28; accepted 2008 August 4)

Abstract

We present results of multi-epoch VLBI observations with VERA (VLBI Exploration of Radio Astrometry) of the 22 GHz H₂O masers associated with a young stellar object (YSO) IRAS 22198+6336 in a dark cloud L1204G. Based on the phase-referencing VLBI astrometry, we derive an annual parallax of IRAS 22198+6336 to be 1.309 ± 0.047 mas, corresponding to the distance of 764 ± 27 pc from the Sun. Although the most principal error source of our astrometry is attributed to the internal structure of the maser spots, we successfully reduce the errors in the derived annual parallax by employing the position measurements for all of the 26 detected maser spots. Based on this result, we reanalyze the spectral energy distribution (SED) of IRAS 22198+6336 and find that the bolometric luminosity and total mass of IRAS 22198+6336 are $450L_{\odot}$ and $7M_{\odot}$, respectively. These values are consistent with an intermediate-mass YSO deeply embedded in the dense dust core, which has been proposed to be an intermediate-mass counterpart of a low-mass Class 0 source. In addition, we obtain absolute proper motions of the H₂O masers for the most blue-shifted components. We propose that the collimated jets aligned along the east-west direction are the most plausible explanation for the origin of the detected maser features.

Key words: Astrometry: — ISM: individual (L1204G) — ISM: jets and outflows — masers (H₂O) — stars: individual (IRAS 22198+6336)

1. Introduction

One of the crucial issues in astronomy and astrophysics is to understand formation processes of stars, planetary systems, and their clusters. They are the most basic constituents in the Galaxy and hence, play essential roles in its formation and evolution. In order to understand physics and dynamics in the star-formation processes, it is necessary to obtain accurate physical properties of target sources such as size, mass, and luminosity. Because all of these values strongly depend on the adopted distance, the distance is the most fundamental parameter for quantitative discussion.

In spite of its importance, however, it has long been difficult to measure accurate distances to star-forming regions without assumptions. The most reliable and direct way to determine the distance is an annual trigonometric parallax method, based on precise measurements of the position and motion of the object. In 1990's, the Hipparcos satellite measured annual parallaxes for more than 100 000 stars with a typical precision of 1 mas level (Perryman et al. 1997). Nevertheless, accurate distance measurements with Hipparcos for star-forming regions were limited to nearby sources within a few hundred pc from the Sun (e.g. Lombardi et al. 2008). Although distances to several OB clusters associated with nearby star-forming regions up to ~ 600 pc have been reported (de Zeeuw et al. 1999), Hipparcos could not directly determine the distances to newly born stars deeply embedded in dusty molecular cloud cores, because Hipparcos was capable of observing only in the optical wavelengths.

In the last few years, phase-referencing VLBI astrometry has been developed drastically, yielding the annual parallaxes of nearby star-forming regions. For instance, radio continuum sources in the Taurus (Loinard et al. 2005; Loinard et al. 2007; Torres et al. 2007), Ophiuchus (Loinard et al. 2008), and Orion (Sandstrom et al. 2007; Menten et al. 2007) regions were observed with the NRAO Very Long Baseline Array (VLBA) to derive their annual parallaxes with typical uncertainty of better than a few percent.

In addition, we have started the initial scientific project "Measurements of annual parallaxes of nearby molecular clouds" with VERA (VLBI Exploration of Radio Astrometry). VERA is a Japanese VLBI network dedicated to astrometric observations aimed at revealing 3-dimensional structure of the Galaxy (Honma et al. 2007; Sato et al. 2007; Sato et al. 2008). In our project for nearby molecular clouds, we specially focus on the accurate distance measurements of star-forming regions within 1 kpc from the Sun (Dame et al. 1987). Our results will contribute to refine all of the observational studies on nearby star-forming regions by providing their most accurate and directly measured distances. We have already conducted astrometric observations of the H₂O maser sources in the Orion (Hirota et al. 2007), Ophiuchus (Imai et al. 2007), and Perseus (Hirota et al. 2008) regions. All of the results provide direct measurements of their distances with much higher accuracy than the previ-

ous photometric methods and the parallax measurements with Hipparcos.

As a part of this project, we present results of astrometric observations of the H₂O maser source IRAS 22198+6336 in a nearby dark cloud core L1204G¹.

L1204 is located in the Cepheus-Cassiopeia molecular cloud complex (Yonekura et al. 1997) and is associated with a well known high-mass star-forming region S140. It is also identified to be a molecular cloud WB176 (Wouterloot & Brand 1989). According to the molecular line observations of L1204, it consists of several high density molecular cores labeled by A-G (Tafalla et al. 1993). A deeply embedded YSO IRAS 22198+6336 is associated with one of the dense cores, L1204G, and it is identified to be a powering source of molecular outflow (Fukui 1989; Wilking et al. 1989). The centimeter and millimeter counterpart of IRAS 22198+6336 is detected with the VLA (Sánchez-Monge et al. 2008). The H₂O masers were detected (Palla et al. 1991) and their distributions were investigated by the VLA (Tofani et al. 1995) and VLBA (Migenes et al. 1999). However, they did not measure the proper motions of the H₂O masers because observations by Tofani et al. (1995) could not achieve sufficient high resolution and Migenes et al. (1999) observed only at 1 epoch. Therefore, the kinematics of the circumstellar materials around IRAS 22198+6336 remains still unclear.

The distance to L1204 is estimated by a photometric method to be 910 pc (Crampton & Fisher 1974) assuming that a B0V star HD211880 is the ionization source of the HII region S140, which is also associated with L1204. On the other hand, de Zeeuw et al. (1999) identified HD211880 (HIP110125) as a member of the Cepheus OB2 cluster. Using the Hipparcos data, de Zeeuw et al. (1999) determined the distance to the Cepheus OB2 cluster to be closer value of 615 ± 35 pc from the Sun. The kinematic distance of 1.3 kpc is sometimes adopted in several literatures (Wouterloot & Brand 1989; Molinari et al. 1996) according to the systemic velocity of -11 km s^{-1} (Tafalla et al. 1993). Depending on the adopted distance, the luminosity of IRAS 22198+6336 could differ by a factor of 4, and hence, its physical properties sometimes contain large uncertainties.

Based on our accurate astrometric observations with VERA, we will provide the parallactic distance to IRAS 22198+6336 in L1204G, together with the kinematics of the circumstellar gas traced by the H₂O masers. We will also discuss the basic properties of the powering source of the H₂O masers by adopting our new distance to L1204G.

¹ In some literature, IRAS 22198+6336 is called as L1204A (Fukui 1989; Palla et al. 1991; Migenes et al. 1999). However, it is quite confusing because L1204A is identified to be another core associated with the well known massive young stellar object (YSO) S140 IRS1 (Tafalla et al. 1993; Tofani et al. 1995). Thus, we refer to the host of IRAS 22198+6336 as L1204G in this paper according to Tafalla et al. (1993).

2. Observations and Data Analysis

The VERA observations of the H₂O masers (6₁₆-5₂₃, 22235.080 MHz) associated with IRAS 22198+6336 have been carried out since Nov. 2006 at intervals of about 1 month and are still ongoing. We present the results from a total of 9 observing sessions from Nov. 2006 to Dec. 2007 (2006/312, 2006/361, 2007/047, 2007/096, 2007/130, 2007/215, 2007/282, 2007/322, and 2007/353; hereafter an observing session is denoted by year/day of the year). All 4 VERA stations participated in all sessions, providing a maximum baseline length of 2270 km.

Observations were made in the dual beam mode; the H₂O masers associated with IRAS 22198+6336 and a reference source J2223+6249 ($\alpha_{J2000.0} = 22^{\text{h}}23^{\text{m}}18.096661\text{s}$, $\delta_{J2000.0} = +62^{\circ}49'33.80393''$; Petrov et al. 2005) were observed simultaneously (Kawaguchi et al. 2000; Honma et al. 2003; Honma et al. 2008a). The reference source J2223+6249 is separated south from IRAS 22198+6336 by 1.1 degrees. J2223+6249 was detected with the peak flux density of about 200 mJy in all the epochs as shown in Figure 1. Left-handed circular polarization was received and sampled with 2-bit quantization, and filtered using the VERA digital filter unit (Iguchi et al. 2005). The data were recorded onto magnetic tapes at a rate of 1024 Mbps, providing a total bandwidth of 256 MHz in which one IF channel and the rest of 15 IF channels with 16 MHz bandwidth each were assigned to IRAS 22198+6336 and J2223+6249, respectively. A bright continuum source, 3C454.3, was observed every 80 minutes for bandpass and delay calibration. System temperatures including atmospheric attenuation were measured with the chopper-wheel method (Ulich & Haas 1976) to be 100-500 K, depending on weather conditions and elevation angle of the observed sources. The aperture efficiencies of the antennas ranged from 45 to 52% depending on the stations. A variation of the aperture efficiency of each antenna as a function of elevation angle was confirmed to be less than 10% even at the lowest elevation in the observations (~ 20 degrees). Correlation processing was carried out on the Mitaka FX correlator (Chikada et al. 1991) located at the NAOJ Mitaka campus. For H₂O maser lines, the spectral resolution was set to be 15.625 kHz, corresponding to the velocity resolution of 0.21 km s⁻¹.

Data reduction was performed using the NRAO Astronomical Image Processing System (AIPS). Amplitude and bandpass calibrations were done for the H₂O maser source (IRAS 22198+6336) and reference source (J2223+6249) independently. For phase-referencing, fringe fitting was done with the AIPS task FRING on the phase reference source (J2223+6249), and the solutions were applied to the target source (IRAS 22198+6336). Because the reference source J2223+6249 showed the double-peaked structure in the synthesized images as shown in Figure 1, we carried out self-calibration to correct for the structure effect on the phase calibration. In addition, we applied the results of the dual-beam phase calibration, in which difference between instrumentally added phases in the two beams

were measured by injecting artificial noise sources into both beams at each station during the observations (Kawaguchi et al. 2000; Honma et al. 2008a). We also corrected for the approximate delay model adopted in the correlation processing. The difference in the optical path length error between our newly applied model and the CALC9 model developed by the NASA/GSFC VLBI group are confirmed to be less than ~ 2 mm. In this correction, drifts of the visibility phase caused by the Earth's troposphere were estimated based on the GPS measurements (Honma et al. 2008b). As discussed in Honma et al. (2008b), the tropospheric zenith delay consists of "dry" and "wet" parts, and only latter one is variable and hence significantly cause the phase errors in the calibrations. The typical tropospheric "wet" zenith delay (path length) was 5-10 cm while it was sometimes as large as 40 cm, in particular at the Ogasawara and Ishigaki stations in summer. On the other hand, the "dry" component of the tropospheric zenith delay was stable about 2.3 m.

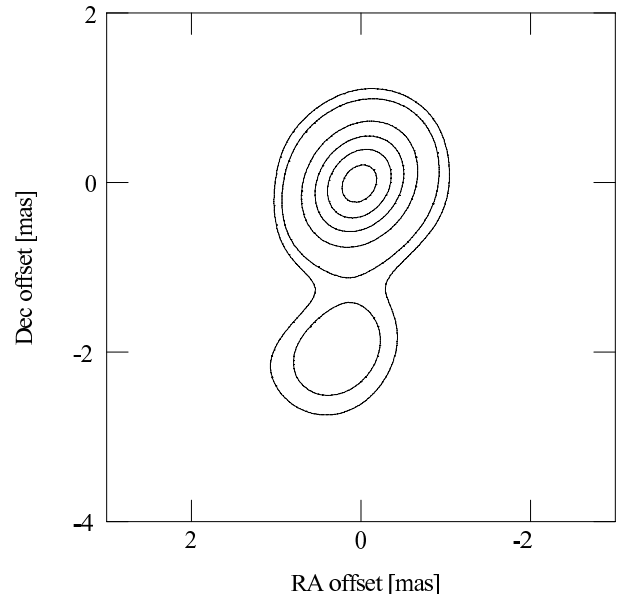


Fig. 1. Self-calibrated image of the reference source J2223+6249 at the first epoch, 2006/312. The contour levels are 5, 10, 30, 50, 70, and 90% of the peak intensity (205.3 mJy beam⁻¹).

Synthesis imaging and deconvolution (CLEAN) were performed using the AIPS task IMAGR with the uniform weighting to achieve the highest spatial resolution, allowing us to resolve complex spatial structures of the masers. The resultant synthesized beam size (FWHM) was typically 1.2 mas \times 0.9 mas with a position angle of -40 degrees. The peak positions and peak flux densities of masers were derived by fitting elliptical Gaussian brightness distributions to each image using the AIPS task SAD. The formal uncertainties in the maser positions given by SAD were mostly better than 0.05 mas.

3. Results

3.1. Overall Properties of the H₂O Masers in IRAS 22198+6336

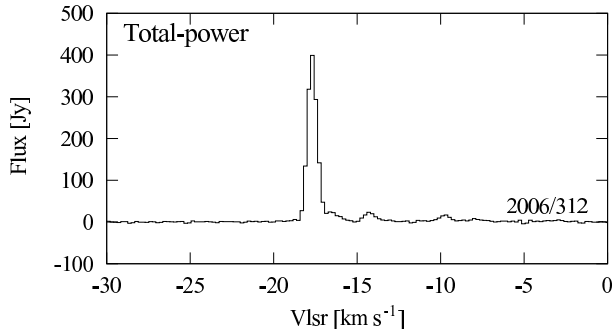


Fig. 2. Total-power spectrum of the H₂O masers associated with IRAS 22198+6336 observed at the first epoch, 2006/312. The spectrum is the average of those observed at all the VERA stations.

Figures 2 and 3 show an example of a total-power spectrum and scalar-averaged cross-power spectra of the H₂O masers associated with IRAS 22198+6336, respectively. The H₂O maser lines were detected within the LSR (local standard of rest) velocity range from -18.5 km s^{-1} to -2.7 km s^{-1} . The intense spectra at the LSR velocity of about -17 km s^{-1} were detected in all the observed epochs, whereas other velocity components were detected at rarer occurrences. In this paper, we refer to the brightest components at -17 km s^{-1} as the main components. Our result is consistent with those of long-term monitoring observations made by Valdetaro et al. (2002) and Brand et al. (2003) that the most prominent maser feature in IRAS 22198+6336 was at the LSR velocity of about -20 km s^{-1} , while those around the systemic velocity of -11 km s^{-1} (Tafalla et al. 1993) rarely appeared. According to their long-term monitoring observations, the radial velocities of the H₂O masers in IRAS 22198+6336 changed with time over the 11-year monitoring period at a rate of $0.2 \text{ km s}^{-1} \text{ yr}^{-1}$. The LSR velocity of the -20 km s^{-1} component has been gradually red-shifted to be about -18 km s^{-1} (Valdetaro et al. 2002; Brand et al. 2003). This trend predicts $\sim -17 \text{ km s}^{-1}$ of the velocity of the main component at around 2007, as observed in our observations. However, we cannot find any signature of the velocity drift within our observing period probably due to our relatively shorter time span.

Since the spectrum taken at the first epoch, 2006/312, showed most of the velocity components, we first searched for the H₂O masers at the first epoch by producing the synthesized images for all the individual velocity channels with the field of view of $\sim 4'' \times 4''$. As a result, we found roughly 4 clusters of maser spots, or features, spreading over the $300 \text{ mas} \times 300 \text{ mas}$ region. Hereafter we define a “spot” as emission occurring in a single velocity channel and a “feature” as a group of spots which are spatially coincident within the beam size and are detected for at

least two consecutive velocity channels. Based on this coarse map, we again carried out synthesis imaging for all the epochs with the field of view of $25.6 \text{ mas} \times 25.6 \text{ mas}$ centered at the positions for each of the identified features.

The results of the mapping are shown in Figure 4, and examples of phase-referenced channel maps are shown in Figure 5. We labeled the groups of features A-M in the order of their LSR velocities. Some of the weak components were not detected in the phase-referenced maps but only detected in the self-calibrated images, in which we carried out phase-calibration using the brightest maser spot rather than the reference source J2223+6249, due to the lower dynamic range of the phase-referenced images. For such spots, we derived their absolute positions by referencing to the absolute position of the brightest spot in the main component that is significantly detected in the phase-referenced images at all the epochs.

The maser distribution shows roughly a circular structure with the radius of about 150 mas as seen in Figure 4(a). Overall spatial and radial velocity distribution of H₂O maser features are in good agreement with those by the VLA (Tofani et al. 1995) and the VLBA (Migenes et al. 1999), but we resolve the previously detected components into several spatially distinct maser spots due to our higher spatial resolution. The main components which are most blue-shifted and brightest, J-M, coincide with both the position and velocity of the C2 component labeled by Tofani et al. (1995), while the most red-shifted components, A-B, coincide in the position and velocity with the C4 component of Tofani et al. (1995). The northern components near the systemic velocity, F-I, are also coincident with both the position and velocity of the C1 component of Tofani et al. (1995). On the other hand, another group of components C-E is spatially coincident with C3 of Tofani et al. (1995), whereas their LSR velocities, from -7 to -10 km s^{-1} , are significantly red-shifted by more than 5 km s^{-1} . Here we emphasize that the accuracy of our absolute positions with an uncertainty of only 1 mas, which is limited mainly by the position uncertainty of the reference source J2223+6249, 0.90 mas and 1.31 mas in right ascension and declination, respectively (Petrov et al. 2005), are about two orders of magnitude higher than those by the previous VLA observations (Tofani et al. 1995) and by the fringe-rate maps obtained with the VLBA (Migenes et al. 1999).

The properties of the features A-I are summarized in Table 1. These parameters are derived from the phase-referenced images except for the two features, D and E, as noted in Table 1. They are compact and almost no significant spatial structures, and hence, we only summarize the parameters for the peak spot in each feature. All of the features listed in Table 1 were detected each only at a single one different epoch probably due to their high variability.

On the other hand, the brightest main features, J-M, show complex spatial structures. We summarize the parameters for the selected 26 spots in Table 2, which are detected in at least three epochs, and hence, are able to obtain reliable proper motions as discussed later.

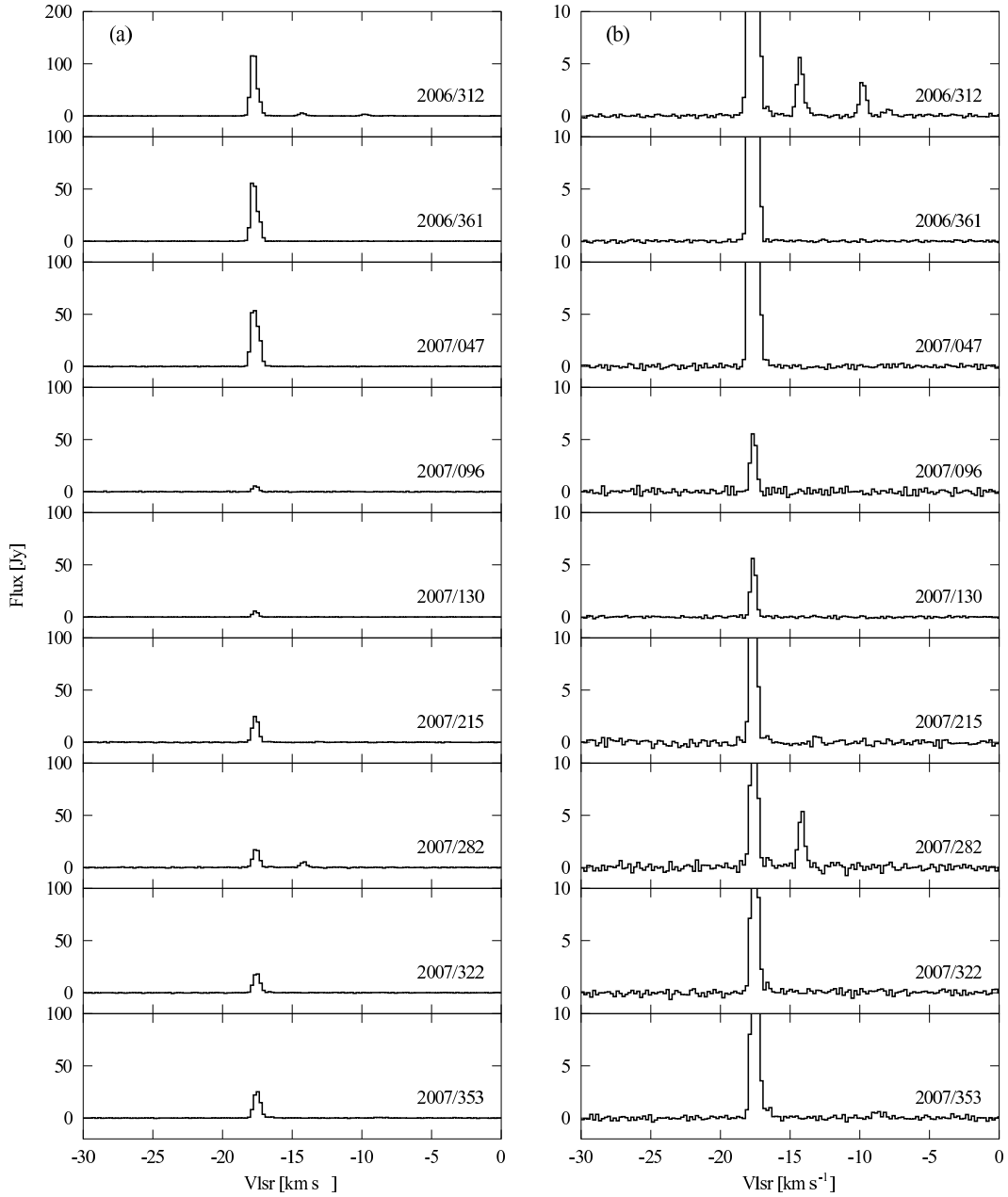


Fig. 3. (a) Scalar-averaged cross-power spectra of the H_2O masers associated with IRAS 22198+6336. The spectra are the averages of those observed at all the VERA stations. Note that the scale of the ordinate for the 2006/312 epoch is twice as large as others. (b) Same as (a) but magnified by a factor of 10 to clarify the weaker spectral components.

The parameters for the spots L1-3 are derived from the self-calibrated images while others are from the phase-referenced images. The main features are resolved into four subgroups; J (4 mas, -23 mas), K (15 mas, 20 mas), L (-1 mas, -12 mas), and M (-1 mas, -3 mas) in right ascension and declination, respectively, and all of them consist of multiple spots. In particular, the component M shows the elongated structure along the north-south direction from 0 mas to -6 mas in declination, as shown in Figures 6 and 5. The relatively large scale structures found in these features have been inferred from the fact that the H_2O masers are highly resolved-out with the

longer baselines in the VLBA (Migenes et al. 1999). We also found that the flux densities of the cross-power spectra of the masers are typically only about 30% of those of the total-power spectra as shown in Figures 2 and 3, which are suggestive of the missing flux. Although the peak velocities of the main features, -17 km s^{-1} were stable, their internal structures were found to be highly variable. The features K and L appeared later than 2007/215, while M was detected only at the earlier epochs than 2007/215. In contrast, the feature J was highly variable but detected throughout whole of the observing period.

As depicted in Figure 4(a), we found a radial velocity

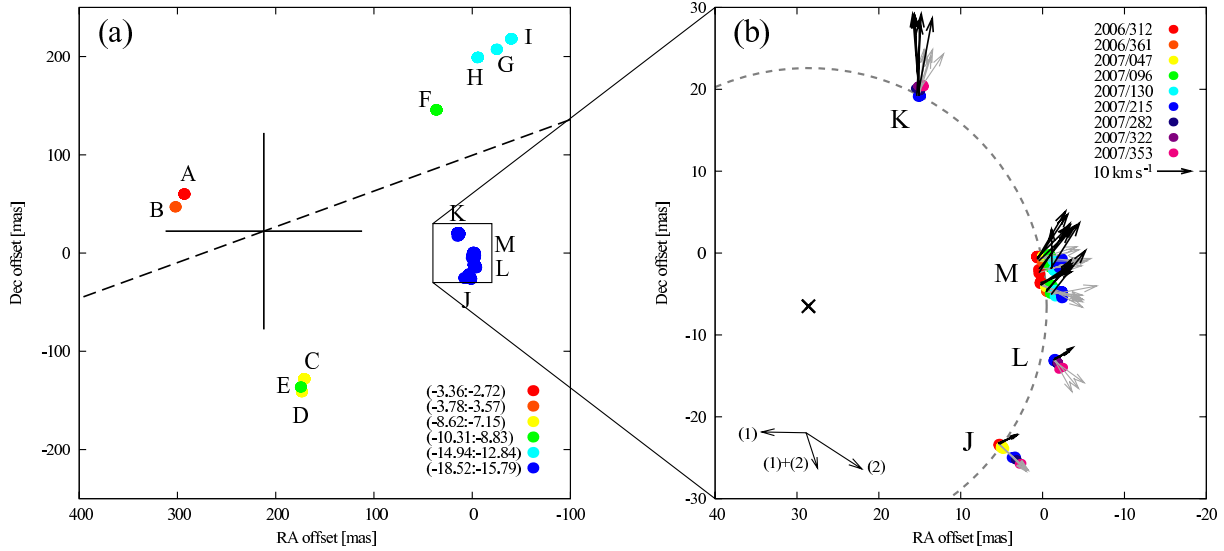


Fig. 4. Phase-referenced maps of the H₂O masers associated with IRAS 22198+6336. (a) Overall distribution of the H₂O maser spots. All the detected spots for all of the 9 observing epochs are plotted. The position offsets in right ascension and declination are measured with respect to the (0,0) position at $\alpha(J2000.0) = 22^{\text{h}}21^{\text{m}}26.72790^{\text{s}}$, $\delta(J2000.0) = +63^{\circ}51'37.9239''$. A cross and a dashed line indicate the peak position and the direction of its elongation of the 7 mm radio continuum emission (Sánchez-Monge et al. 2008), of which error bar is roughly estimated from the beam size and signal-to-noise ratio of the VLA observation. (b) Distribution and proper motions of the maser spots in the main features J-M. The movements of the spots indicated by the color-coded filled circles represent the absolute proper motions without correction of the Solar motion and Galactic rotation. Grey arrows represent the absolute proper motions whereas the thick black arrows represent the proper motions corrected for the Solar motion and the Galactic rotation. The proper motion of 1 mas yr⁻¹ corresponds to 3.6 km s⁻¹, and the proper motion vector of 10 km s⁻¹ is shown in the top left of this figure. The arrows shown in the bottom-left corner represent the magnitude of (1) the Solar motion (3.612 mas yr⁻¹, 0.064 mas yr⁻¹), (2) the Galactic rotation (-4.543 mas yr⁻¹, -2.947 mas yr⁻¹), and the sum of (1) and (2). A large circle indicates the best fit model of the possible expanding shell model (see text).

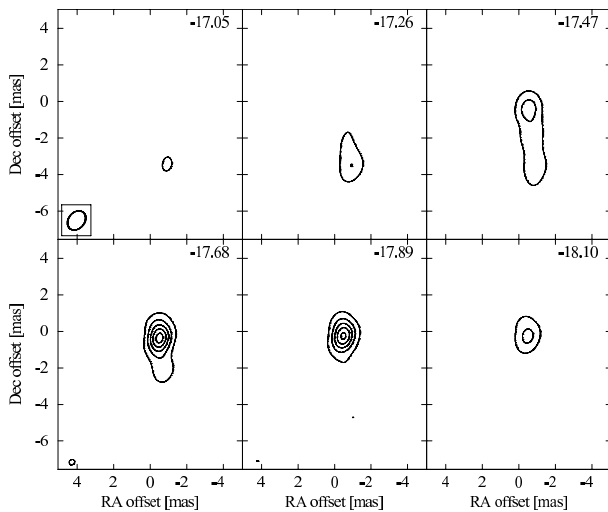


Fig. 5. Examples of phase-referenced channel maps of the elongated maser features M at the first epoch, 2006/312. Contour levels are 10, 30, 50, 70, and 90% of the peak intensity (112.2 Jy beam⁻¹). The LSR velocities are indicated at the top-right corner of each panel, in unit of km s⁻¹. The beam size is shown in the top-left panel.

gradient along the east-west direction when we consider the clusters of features A-B and J-M; blue-shifted (J-M) and red-shifted (A-B) components tend to be distributed at the western and eastern sides of the map, respectively.

The similar radial velocity gradient has been reported by Tofani et al. (1995) and Miggenes et al. (1999) which is attributed to the bipolar outflow. On the other hand, the larger-scale ($>1'$) velocity gradient along the northwest-southeast direction has been found in the spectral line observations of NH₃ (Tafalla et al. 1993) and C¹⁸O (Jenness et al. 1995). Although they attributed these velocity gradients to the molecular outflow, their velocity structures showed an opposite trend to our H₂O maser distribution; the blue-shifted and red-shifted components traced by the NH₃ and C¹⁸O lines tend to be located at southeast and northwest, respectively. It would be suggested that the large-scale velocity gradient does not directly related to that traced by the H₂O masers. Detailed discussion about the spatial and velocity structures of the H₂O masers will be presented later.

3.2. Astrometry of the H₂O Masers

We conducted monitoring observations of the H₂O masers for about one year, and the absolute motions of the maser spots were successfully obtained by referencing to the extragalactic position reference source J2223+6249. The movement of each maser spot can be expressed by the sum of a linear motion and the annual parallax. It can be assumed that all the maser features or spots in L1204G have the same annual parallax within the astrometric accuracy of VERA. Therefore, we can simultaneously determine the proper motions ($\mu_{\alpha}^i \cos \delta$, μ_{δ}^i) and the initial

Table 1. The peak maser spots in the features A-I

No	v_{lsr} [km s ⁻¹]	Detected Epoch	$\Delta\alpha$ [mas]	$\Delta\delta$ [mas]	F_{peak} [Jy beam ⁻¹]
A	-3.15	2006/312	293.43	60.22	1.9
B	-3.57	2006/312	302.30	47.19	0.74
C	-8.20	2006/312	171.42	-128.00	3.9
D ^a	-8.41	2007/353	173.85	-141.05	2.2
E ^a	-8.83	2007/353	174.73	-136.19	2.7
F	-9.68	2006/312	36.88	145.81	11.5
G	-13.05	2007/215	-24.59	207.43	1.9
H	-14.31	2006/312	-5.22	199.21	15.7
I	-14.31	2007/353	-39.40	218.13	7.2

Note — All the features are detected only at the epoch noted in the third column. The brightest spots in each feature are listed.

a: The spots are detected only in the self-calibrated images.

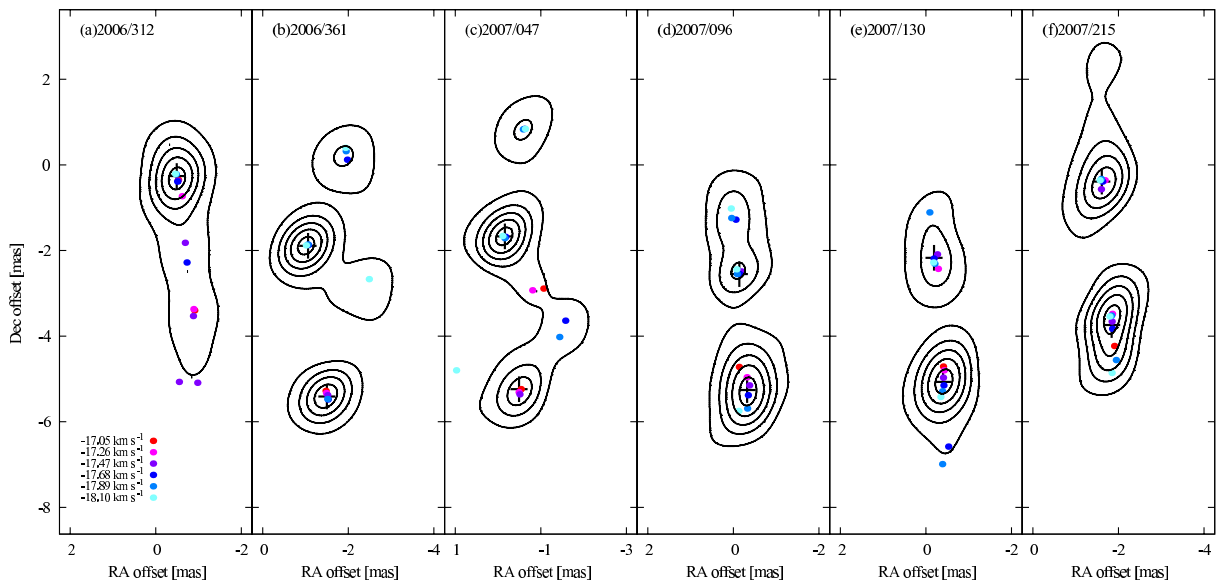


Fig. 6. Structures of the elongated maser features M obtained by integrating the phase-referenced channel maps. Contour maps show the integrated flux densities of the features with the contour levels of 10, 30, 50, 70, and 90% levels of the peak flux densities. Peak values are 329.9 Jy beam⁻¹, 60.0 Jy beam⁻¹, 52.0 Jy beam⁻¹, 13.1 Jy beam⁻¹, 26.1 Jy beam⁻¹, and 16.2 Jy beam⁻¹, for (a)2006/312, (b)2006/361, (c)2007/047, (d)2007/096, (e)2007/130, and (f)2007/215, respectively. Crosses represent the positions and their error bars for the features employed in the datasets 3 and 4 (see Table 3), while color-coded filled circles represent the positions of the spots.

positions (α_0^i , δ_0^i) in right ascension and declination for the i -th feature or spot, along with a common annual parallax of L1204G, π , by the least-squares analysis of all the detected features or spots. Because only the features in the main components, J-M, were detected at more than two epochs, we excluded the features A-I in the following astrometric analysis.

To obtain the accurate annual parallax, we attempted to analyze the data by adopting four different datasets; (1) both the right ascension and declination data for all the spots, (2) only the right ascension data for all the spot, (3) same as (1) but for all the features, and (4) same as (2) but for all the features. As already defined, the fea-

ture is the sum of the spatially coincident maser spots integrated over at least two consecutive velocity channels. Thus, we determined the peak position of each feature by the Gaussian fitting of the velocity-integrated phase-referenced intensity map. On the other hand, the peak position of each spot is derived from the individual channel map obtained from the phase-referenced analysis by assuming that the velocity of the maser spot is constant, i.e. the maser spots are regarded to be identical if their velocities are the same. It would not always be valid if the masers show significant velocity drift (Hirota et al. 2008). However, we applied this assumption to the identification of the detected spots between different epochs because we

Table 2. All the maser spots in the main features J-M used for the parallax measurement

No	v_{lsr} [km s ⁻¹]	Detected Epochs	$\Delta\alpha$ [mas]	$\Delta\delta$ [mas]	F_{peak} [Jy beam ⁻¹]	$\mu_\alpha \cos \delta$ [mas yr ⁻¹]	μ_δ [mas yr ⁻¹]
J1	-16.42	1*3**67*9	4.15	-23.17	3.7	-2.33(25)	-2.32(32)
J2	-16.63	1*3**67*9	4.14	-23.31	6.4	-2.48(25)	-2.20(32)
J3	-16.84	1*3**67*9	4.03	-23.33	3.0	-2.27(25)	-2.10(32)
K1	-17.05	*****789	14.21	20.60	2.7	-2.02(168)	3.00(213)
K2	-17.26	*****6789	15.53	20.48	4.7	-0.99(83)	3.18(105)
K3	-17.47	*****6789	15.51	20.44	8.2	-0.58(83)	3.71(105)
K4	-17.68	*****6789	15.48	20.46	8.5	-0.55(83)	3.71(105)
K5	-17.89	*****6789	15.51	20.46	6.8	-0.40(83)	3.79(105)
K6	-18.10	*****67*9	15.62	20.36	2.7	-1.29(88)	3.80(110)
L1 ^a	-17.68	*****6789	-0.99	-11.88	12.8	-1.45(83)	-2.63(105)
L2 ^a	-17.89	*****6789	-0.95	-11.94	10.1	-2.53(83)	-1.85(105)
L3 ^a	-18.10	*****6789	-1.02	-11.77	2.5	-2.00(83)	-2.44(105)
M1	-17.05	123456***	-0.90	-3.40	19.6	-3.44(41)	-2.00(50)
M2	-17.26	123456***	-0.88	-3.37	60.2	-3.45(41)	-1.23(50)
M3	-17.47	123456***	-0.87	-3.53	48.8	-3.43(41)	-1.35(50)
M4	-17.68	*2*456***	-1.52	-5.48	10.4	-2.98(55)	-0.75(69)
M5	-17.89	*2*456***	-1.51	-5.47	8.9	-2.96(55)	-0.26(69)
M6	-18.10	***456***	-0.12	-5.75	0.6	-3.73(98)	0.70(125)
M7	-17.47	1**456***	-0.68	-1.82	42.6	-3.49(45)	0.26(55)
M8	-17.68	1**456***	-0.72	-2.28	20.4	-3.44(45)	1.11(55)
M9	-17.89	***456***	-0.08	-2.55	1.2	-3.28(98)	0.83(125)
M10	-18.10	*2*456***	-2.48	-2.67	3.3	-0.90(55)	0.30(69)
M11	-17.05	1*3**6***	-0.52	-0.35	2.7	-3.89(45)	-0.01(56)
M12	-17.68	1234*****	-0.50	-0.39	175.7	-3.39(78)	0.80(96)
M13	-17.89	12345*****	-0.47	-0.22	146.1	-3.62(60)	-0.24(72)
M14	-18.10	1234*****	-0.45	-0.21	59.5	-3.24(78)	0.99(96)

Note — In the third column, the numbers indicate the detected epochs corresponding to 1; 2006/312, 2; 2006/361, 3; 2007/047, 4; 2007/096, 5; 2007/130, 6; 2007/215, 7; 2007/282, 8; 2007/322, and 9; 2007/353, respectively. The epoch in which the maser is not detected is indicated by an asterisk instead of above number. Positions and flux densities are those observed at the epoch detected for the first time, as noted in the third column. Numbers in parenthesis represent the errors in unit of the last significant digits.
^a: In the epochs of 2007/322 and 2007/353, the spots are detected only in the self-calibrated images.

could not find significant velocity drift in our observations as mentioned above.

Comparison of former and latter datasets shows the effect of the structures in the maser features on our astrometric accuracy. As mentioned above, we found significant spatial structures in the features J-M. In particular, the elongated structure in the feature M can be clearly seen in Figure 6, in which the peak positions of the maser spots do not always coincide with those of the features. These complex spatial and velocity structures within the feature M would degrade the accuracy of astrometry as reported in the previous results of VERA for nearby sources (Hirota et al. 2007; Hirota et al. 2008; Imai et al. 2007). Instead, we resolved the internal structure of the feature M by producing the channel maps of all the velocity components. They could better trace the motion of the masing gas in the multi-epoch astrometric analysis. According to their positions and velocity channels, we identified in total 5 features (1 in feature J-L for each and 2 in feature

M) and 26 spots in the main components J-M as listed in Table 2, which were detected in at least three observing epochs. Some of the spots, for instance, the spots J1-3, K6, M4-5, M7-8, and M10-11, were not always detected probably due to the variability and the insufficient sensitivity. However, our identification of the maser spots is proved to be appropriate because their motions are well fitted to the linear proper motions and annual parallax which is common for other spots, as shown in Figure 7. Thus, all of the proper motions identified in our analysis really trace the bulk motion of the masing gas.

In addition, we evaluate the effect of the atmospheric zenith delay residual by comparing the datasets 1 and 3 with those of datasets 2 and 4. According to the previous results with VERA (Honma et al. 2007; Hirota et al. 2007; Hirota et al. 2008; Imai et al. 2007), the accuracy of the derived annual parallax is significantly improved when only the data for right ascension are used, as this data is less affected by atmospheric modeling errors. Therefore,

we ran the fitting by making use of right ascension data alone and both right ascension and declination data for comparison.

All the results for different four datasets can be compared in Table 3. The results of the fitting are also displayed in Figure 7 for the dataset 1. The standard deviations of the post-fit residuals are ~ 0.2 mas and ~ 0.3 mas in right ascension and declination, respectively. If we employ the formal uncertainties in the Gaussian fitting of the maser spots, ~ 0.05 , as the positional errors in our observations, a reduced- χ^2 is as large as 20. This result would suggest that we underestimate the positional errors and that these post-fit residuals represent the actual positional accuracy of the astrometric observations with VERA. Thus, we took into account σ_α and σ_δ listed in Table 3 in the least-squares analysis to give a weight, which is inversely proportional to the square of the error, for the right ascension and declination data, respectively.

As can be seen in Table 3, all of the 4 datasets yield the consistent parallax values within the mutual errors. Although none of the spots were persistent during whole of the observing period due to their variability, we could determine the annual parallax with an uncertainty of smaller than 10% by successfully identifying multiple spots during almost 1 year. The highest accuracy is achieved by adopting both right ascension and declination data for all of the 26 detected spots, dataset 1. The resultant value of the annual parallax for the dataset 1 is 1.309 ± 0.047 mas, corresponding the distance to IRAS 22198+6336 of 764 ± 27 pc. The associated uncertainties of only $\sim 4\%$ for the dataset 1 is smaller than the others, and this dataset provides the most reliable value. Detailed discussions about the possible astrometric error sources will be presented in the section 4.1.

Along with the annual parallax, proper motions of the maser spots are derived, as summarized in Table 2 and illustrated in Figure 4(b). The proper motion of 1 mas yr^{-1} corresponds to 3.6 km s^{-1} at the distance of 764 pc. Although the proper motions for some of the features contain large uncertainties, we can see a systematic trend in the direction and magnitude of the proper motion vector in Figure 4(b). The kinematics traced by the proper motions as well as the radial velocities of the masers will be discussed in the section 4.4.

4. Discussions

4.1. Astrometric Error Sources

As discussed in the recent works on astrometry with VLBA and VERA (Hachisuka et al. 2006; Honma et al. 2007), it is difficult to estimate individual error sources induced in the VLBI astrometry quantitatively. In this paper, we regard the post-fit residuals of the least-squares analysis listed in Table 3 as the typical positional errors, which results in a reduced- χ^2 of unity. Because they are significantly larger than the formal uncertainties in the Gaussian fitting of the maser spots, ~ 0.05 mas, some systematic errors would have significant effects on the astrometry. Here we discuss about the possible error sources

in the present results.

One of the serious error sources is the atmospheric zenith delay residuals mainly due to the tropospheric water vapor. This effect is caused by the difference in the optical path lengths through the atmosphere between the target and reference sources because their elevation angles are usually different. Honma et al. (2008b) presented results of detailed simulations to calculate the positional errors caused by the atmospheric zenith delay residuals in astrometry with VERA. They demonstrated that the positional error due to the zenith delay residual of 2 cm, which is a typical value of VERA observations, is better than 0.030 mas and 0.018 mas for right ascension and declination, respectively, in the case of the declination of 60 degrees, separation angle (SA) between the two sources of 1 degree, and the position angle (PA) on the sky from the target source to the reference source of 180 degrees, which are valid for the IRAS 22198+6336 and J2223+6249 pair aligned along the north-south direction. It turns out that the simulated positional error for this pair cannot fully explain the observed positional uncertainties, unless we introduce an unrealistically large scatter of the zenith delay residual of ~ 30 cm for each of the observation. Therefore, it is unlikely that the atmospheric zenith delay residuals is the most dominant source of our astrometric errors.

Alternatively, we propose that the principal error source in the present results would be the temporal variation of the internal structure of the masers, as proposed by some previous results from the VERA astrometry (Hirota et al. 2007; Hirota et al. 2008; Imai et al. 2007). This effect would be more serious for nearby sources than the distant ones. In fact, we can see spatial structure of the features in Figure 6, and some of the spots in Figure 7 show significant deviations from the best fit model. Even in the case of the fitting of the spots rather than the features, the internal structures in the individual spots might be still significant. Although this effect would limit the positional accuracy of each observation, the accuracy of the annual parallax measurements can be improved with increasing number of spots used in the analysis if the variation of the structure behaves in the random way. Indeed, the post-fit residuals are reduced almost inversely proportional to the square root of the degrees of freedom in the fitting as listed in Table 3.

On the other hand, we confirmed that the uncertainties in the station positions, path length errors due to ionosphere, and the delay model employed in our data analysis, which is consistent with the CALC9 model, would have negligible effects on our astrometry with VERA (Honma et al. 2007). The uncertainties in the absolute position of the reference source J2223+6249, 0.90 mas and 1.31 mas in right ascension and declination, respectively (Petrov et al. 2005), do not affect the derived annual parallax and proper motion because they would add only a constant offset to the position of the maser features. The spatial structure and its temporal variation of the reference source J2223+6249 possibly contribute to the positional errors of the maser features. However the structure effect of the reference source would be much less significant than

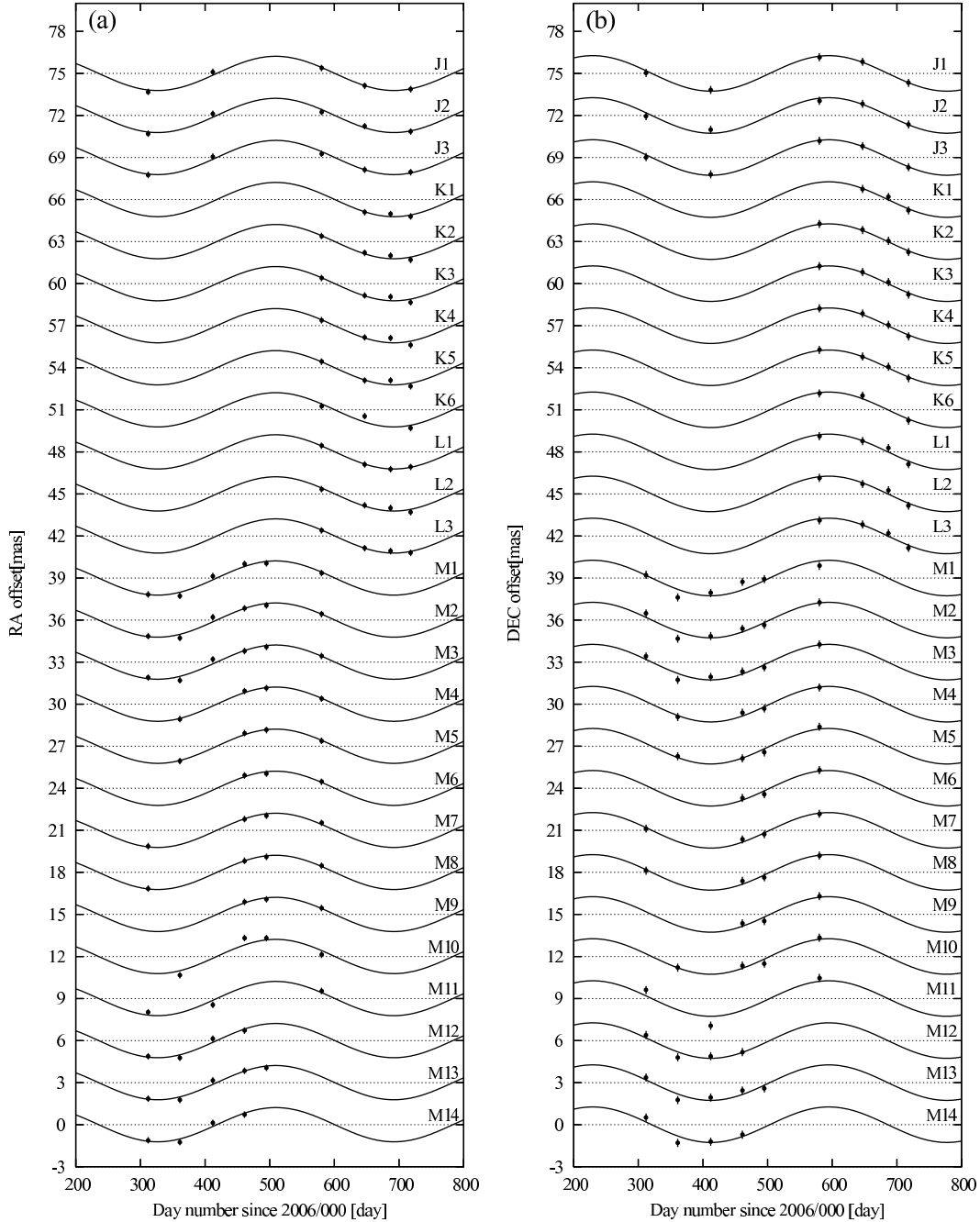


Fig. 7. Position measurements of the maser spots in the features J-M. (a) The movement in right ascension as a function of time. Solid lines represent the best fit model of the annual parallax which are common for all the spots. The best fit proper motions are removed, and hence, the curves represent the modulation in the positions due to the annual parallax. Filled circles represent the observed positions of the maser spots. (b) The same as (a) in declination. The associated error bars, 0.23 mas and 0.29 mas in right ascension and declination, respectively, are also plotted but cannot be seen in the figures.

those of the masers because we performed self-calibration of J2223+6249 to solve its structure. According to the dynamic range of the self-calibrated image of J2223+6249 (~ 20 ; Figure 1), the positional uncertainty caused by the structure of the reference source would be less than 0.025 mas (HPBW/2SNR where HPBW and SNR represent the synthesized beam width and signal-to-noise ratio, respectively).

In summary, we conclude that the astrometric accuracy in our observations is mainly limited by the structure of the maser features, and that the atmospheric zenith delay residuals also contribute to some extent to the error sources. As suggested by Honma et al. (2008b), tropospheric zenith delay residual also plays as a random error because they are correlated only over a few days. Thus, one can reduce the post-fit residuals by employing longer

Table 3. Summary of the least-squares analysis for the annual parallax measurements

Parameter	Dataset 1	Dataset 2	Dataset 3	Dataset 4
Dataset	RA and Dec 26 spots	RA only 26 spots	RA and Dec 5 features	RA only 5 features
Total number of data	218	109	52	26
Numbers of fitted parameters	105	53	21	11
Degrees of freedom	113	56	31	15
π (mas)	1.309(47)	1.289(66)	1.243(80)	1.288(107)
D (pc)	764(27)	776(40)	805(52)	777(65)
σ_α (mas)	0.23	0.23	0.22	0.23
σ_δ (mas)	0.29	—	0.32	—

Note — Numbers in parenthesis represent the errors in unit of the last significant digits. σ_α and σ_δ are the rms deviations of the post-fit residuals in the right ascension and declination directions, respectively.

observing epochs as well as using larger number of masers. Thus, the longer monitoring observatio will be helpful to achieve higher precision and accuracy of the parallax measurements, which is still underway.

4.2. Distance to IRAS 22198+6336 in L1204G

We derived the distance to L1204G to be 764 ± 27 pc from the Sun. This value is smaller than the earlier photometric result, 910 pc (Crampton & Fisher 1974), and the kinematic distance, 1.3 kpc (Wouterloot & Brand 1989; Molinari et al. 1996). While they did not report the errors in the derived distances, photometric and kinematic distances would generally contain larger uncertainties by a factor of a few tens of percent than the parallactic distances (e.g. Hirota et al. 2008, Sato et al. 2008, and references therein). The closer distance, 615 ± 35 pc, is reported by de Zeeuw et al. (1999) based on the Hipparcos measurements of the annual parallaxes of the Cepheus OB2 cluster members, in which one of the members HD211880 is the ionization source of S140 that is possibly associated with L1204. This value is offset from our measured distance of IRAS 22198+6336 by 149 ± 44 pc and is slightly larger than the apparent diameter of the Cepheus OB2 cluster of about 130 pc (~ 12 degrees in the plane of the sky; de Zeeuw et al. 1999). If L1204G is physically associated with the Cepheus OB2 cluster, our result suggests that L1204G would be located at the farthest side of the Cepheus OB2 cluster. Our parallactic distance to IRAS 22198+6336 is found to be very close to the well studied H₂O maser sources in the Cepheus-Cassiopeia region such as IC1396N (Patel et al. 2000) and Cepheus A (Torrelles et al. 2001), although they are not based on the parallax measurements. Together with parallactic distances of the maser sources in this region including NGC281 reported by Sato et al. (2008) and further measurements such as for IC1396N and Cepheus A, we will be able to reveal the 3-dimensional structure of this molecular cloud complex and refine the statistical studies of star-formation in this region (Yonekura et al. 1997).

4.3. Physical Properties of IRAS 22198+6336

Although the adopted FIR luminosity of IRAS 22198+6336 is different from literature to literature, it has been included in the sample of massive YSOs judging from the relatively large far-infrared or bolometric luminosity (Palla et al. 1991; Molinari et al. 1996; Sánchez-Monge et al. 2008). For instance, Tafalla et al. (1993) adopted L_{IRAS} to be $250L_\odot$ while Tofani et al. (1995) adopted L_{FIR} to be $580L_\odot$ by assuming the same distance ~ 900 pc. In contrast, Molinari et al. (1996) assumed the kinematic distance of 1.3 kpc and derived the larger FIR luminosity of $1240L_\odot$. Very recently, Sánchez-Monge et al. (2008) reported results of a survey of millimeter and centimeter continuum emission from high-mass to intermediate-mass YSOs including IRAS 22198+6336, of which they adopted the luminosity of $1300L_\odot$. Based on the radio continuum observations with the VLA of IRAS 22198+6336 along with the observed flux densities reported by previous literatures, Sánchez-Monge et al. (2008) presented basic physical properties of the radio counterpart of the IRAS source, VLA 2, such as mass and luminosity.

However, all of these results employed the larger distances than our present result. Here we refine the physical properties of the possible powering source of the H₂O masers, IRAS 22198+6336 VLA 2, based on our newly derived distance and previously reported flux values by multiplying a scaling factor proportional to an appropriate power of the distance D . For instance, a factor of $(764 \text{ pc}/1300 \text{ pc})^2 = 0.35$ is adopted for correcting the luminosity reported by Sánchez-Monge et al. (2008).

First of all, we stress that the bolometric luminosity is reduced to be $450L_\odot$, which is only 35% of previously adopted value, $1300L_\odot$. Such a low luminosity would argue against a classification of IRAS 22198+6336 as a massive YSO. The derived luminosity set limits on the stellar mass of IRAS 22198+6336. If it is a zero-age main sequence (ZAMS) star, the spectral type of late-B (between B6 and B7) with the stellar mass of about $5M_\odot$ (Stahler & Palla 2004) well accounts for the derived lu-

minosity. On the other hand, if it is in a pure accretion phase, the stellar mass of $7M_{\odot}$ is derived from the accretion luminosity with the typical mass accretion rate of $10^{-5}M_{\odot} \text{ yr}^{-1}$ and the stellar radius of $5R_{*}$ (Stahler & Palla 2004). The newly obtained total (gas+dust) mass of IRAS 22198+6336, $(7-10)M_{\odot}$, which is only 35% of that derived from the SED fitting (Sánchez-Monge et al. 2008), is in good agreement with the above values. Thus, our result implies that IRAS 22198+6336 is not a massive but an intermediate-mass YSO with the mass of no more than $7M_{\odot}$. The lack of the IRAS 12 μm emission as well as no near-infrared counterpart in the 2MASS images support the hypothesis that IRAS 22198+6336 is deeply embedded intermediate-mass YSO, which is analogous to low-mass Class 0 source (Sánchez-Monge et al. 2008).

According to Sánchez-Monge et al. (2008), IRAS 22198+6336 is associated with centimeter radio continuum emission, which could arise either in an ultra-compact HII region or a shock-ionized region in the outflow. They concluded that the contribution of shock-ionized gas around IRAS 22198+6336 should be only a small fraction of the observed centimeter emission because of an extremely high ratio of the centimeter continuum luminosity $S_{\nu}D^2$ to the outflow momentum rate, \dot{P} , with an efficiency factor of 90%. However, if we assume the distance of 764 pc, the ratio is reduced by a factor of 0.59 because the luminosity is proportional to D^2 while the outflow momentum rate, which is usually derived from the linear size, radial velocity, and inclination angle of the outflow, is proportional to D . Even if this is the case, the efficiency of 50% is still higher than the typical low-mass YSOs, $\sim 10\%$ (Anglada 1995), suggesting that it would be significantly higher in the very early-stage of intermediate-mass YSOs.

The mass and luminosity of IRAS 22198+6336 refined by our newly derived distance is consistent with that of the intermediate-mass deeply embedded YSO with the spectral type of late-B. Nondetection of the 6.7 GHz CH_3OH masers, which is thought to be a signpost of massive star-formation site, toward IRAS 22198+6336 (Szymczak et al. 2000) also supports our conclusion that IRAS 22198+6336 is not a massive YSO. Although the OH masers, which is another signature of massive star-formation associated with an ultra-compact HII region, are detected toward IRAS 22198+6336 (Edris et al. 2007), relatively lower resolution of the OH maser observations, $\sim 3'$, might give argument against their association with the same powering source of the H_2O masers. Further observational studies with the higher-resolution and higher-sensitivity centimeter, millimeter, and submillimeter interferometers would shed light on the properties of the central star in L1204G more clearly. Such detailed observational studies on IRAS 22198+6336 would be quite important because it is one of the rare sources in the very early stage of intermediate-mass YSO associated with the H_2O masers (e.g. Patel et al. 2000) and hence, good target sources for the complete understanding of the very early stage of intermediate-mass star-formation processes.

4.4. Kinematics of the Jet Traced by the H_2O masers in IRAS 22198+6336

Together with the annual parallax, we successfully measured the proper motions of the maser spots around IRAS 22198+6336. These results enable us to discuss in detail about the kinematics of the circumstellar materials. Prior to discussions, we should note that the proper motions obtained with VERA do not represent the "intrinsic" proper motions of the masers because they are measured with respect to the Sun and hence, include the contribution of the Solar motion and the Galactic rotation. Assuming the Solar motion relative to the LSR based on the Hipparcos satellite data, $(U_0, V_0, W_0) = (10.00, 5.25, 7.17) \text{ km s}^{-1}$ (Dehnen & Binney 1998), we estimated the contribution of the Solar motion to the observed absolute proper motion to be $3.612 \text{ mas yr}^{-1}$ and $0.064 \text{ mas yr}^{-1}$ in right ascension and declination, respectively. In addition, contributions of the Galactic rotation is calculated to be $(-4.543 \text{ mas yr}^{-1}, -2.947 \text{ mas yr}^{-1})$ on the assumption of the flat rotation with R_0 of 8.0 kpc (Reid 1993) and Θ_0 of 236 km s^{-1} (Reid & Brunthaler 2004) for L1204G at the distance of 764 pc. Subtracting these values from the observed proper motions listed in Table 3 and shown in Figure 4(b), we obtained the intrinsic proper motions of the H_2O masers corrected for the Solar motion and Galactic rotation.

The origin of these proper motions is attributed to either due to the systemic motion of the host cloud L1204G itself, the internal motions of the masers with respect to the powering source IRAS 22198+6336, such as jets and rotating disk associated with it, or both. Regarding to the systemic motion, observed proper motions might trace the peculiar motion of L1204G with respect to the Galactic rotation. The discrepancy between the kinematic distance of L1204G, which is obtained by assuming that L1204G exactly follows the Galactic rotation curve, and our parallactic distance would be suggestive of the effect of the peculiar motion of L1204G rather than the Galactic rotation. Indeed, L1204G ($b \sim 5.7$ degrees) is situated at 75 pc above the Galactic plane with a half-thickness of 87 pc (Dame et al. 1987), which seems too large to apply the flat rotation model. However, the systemic motion of L1204G is quite uncertain because of a lack of the proper motion measurements of IRAS 22198+6336, as suggested in the previous result with VERA of NGC 1333 (Hirota et al. 2008). Therefore, here we only consider several possibilities for the origin of internal proper motions of the masers and the kinematics in the circumstellar material.

As shown in Figure 4(a), the proper motions of the features J-M provide a hint of systematic motion directed outward from the center of the circular structure with the approximate diameter of $\sim 300 \text{ mas}$ or 200 AU. It is naturally interpreted that the most blue-shifted and red-shifted components trace the interacting region with the ambient gas and the collimated jets aligned in the east-west direction, and that the powering source is located at the center of the maser distribution (see Figure 4(a)). This is roughly consistent with the position and elongation

of the VLA source observed at the 7 mm band (Sánchez-Monge et al. 2008), although their spatial resolution is much larger than our VLBI observations. The possible trend of the northward proper motion vectors in Figure 4(b) could be due to the unknown systemic motion of the powering source. The close-up view of the main features shows an arc-like structure indicative of a bow shock, as seen in Figure 4(b). Such bow shock structures at the tips of the collimated jets have been found in low-mass Class 0 protostars IRAS 05413-0104 (Claussen et al. 1998) and S106 FIR (Furuya et al. 2000).

In this case, the origin of the other maser spots close to the systemic velocity, which seem to be distributed perpendicular to the possible jets, would be accounted for by the rotating disk. The radial velocity difference along the north-south direction, $\sim 8 \text{ km s}^{-1}$ and their separation, $\sim 200 \text{ AU}$ ($\sim 300 \text{ mas}$), implies the Keplerian rotation with the centrally enclosed mass of $1.6M_{\odot}/(\cos i)^2$ where i is the inclination angle between the rotation axis and the line-of-sight. The inclination angle of the disk i can be estimated from that of the east-west jets traced by the most blue-shifted and red-shifted masers as follows. The mean proper motions of the most blue-shifted masers are derived to be $-1.53 \text{ mas yr}^{-1}$ and 3.15 mas yr^{-1} in right ascension and declination, respectively. If we adopt the proper motions only in the right ascension direction as the outward velocity of the jets, the mean transverse velocity of 5.5 km s^{-1} toward west and the mean radial velocity of -6.6 km s^{-1} with respect to the systemic velocity for the maser spots J-M give the inclination angle i of 50 degrees. Similarly, if we adopt the proper motions of both the right ascension and declination direction, the mean transverse velocity of 12.6 km s^{-1} yields the inclination angle i of 66 degrees. The enclosed mass is estimated to be $3.9M_{\odot}$ and $9.7M_{\odot}$ for former and latter case, respectively, and these values are almost consistent with the result of the SED fitting $\sim 7M_{\odot}$.

On the other hand, the radio continuum emission in the 1.3 cm and 7 mm bands showed elongated structure along the northwest-southeast direction (Sánchez-Monge et al. 2008). According to their SED analysis, the 1.3 cm emission is dominated by the free-free emission from the shock-ionized jets while the 44% of the 7 mm flux comes from the thermal dust emission in the circumstellar disk, and hence, the 7 mm emission would be due to a superposition of the ionized jet and the dust disk (Sánchez-Monge et al. 2008). The direction of the radio continuum emissions are consistent with that of the large-scale velocity gradient (Tafalla et al. 1993; Jenness et al. 1995), and hence, Sánchez-Monge et al. (2008) attributed them to the free-free emission from the ionized radio jets. However, the large-scale velocity gradient showed opposite trend to our H₂O maser distribution as mentioned in section 3.1. The maser distributions might trace an interface between the ambient material and the outflow lobe which is parallel to the radio continuum source (e.g. Moscadelli et al. 2006), whereas the asymmetric distribution of the masers with respect to the outflow axis cannot be accounted for by the simple model only.

It is worth considering another possibility of the rotating disk around the YSO with a rotation axis along the north-south direction. If we assume the radial velocity gradient along the east-west direction, $\sim 16 \text{ km s}^{-1}$ per $\sim 200 \text{ AU}$ ($\sim 300 \text{ mas}$), as a cause of rotation, the enclosed mass is estimated to be at least $6.4M_{\odot}$, which is comparable to the total mass or stellar mass of IRAS 22198+6336 as discussed in the previous section. In this case, the northern and southern components C-I would trace the jets from the central YSO. Their radial velocity close to the systemic velocity would indicate that the jets are aligned almost within the plane of the sky and hence, the disk is almost edge-on view. The directions of the radio continuum emissions in the 1.3 cm and 7 mm bands (Sánchez-Monge et al. 2008) are in good agreement with that of the H₂O maser features C-I. Nevertheless, this model cannot explain the observed velocity drift of $0.2 \text{ km s}^{-1} \text{ yr}^{-1}$ for the -20 km s^{-1} feature (Valdettaro et al. 2002; Brand et al. 2003) because the velocity drift at the edge of the disk (at the radius of 100 AU) is estimated to be only $0.01 \text{ km s}^{-1} \text{ yr}^{-1}$ in the case of the YSO with the mass of $5M_{\odot}$. Thus, the rotating disk with the axis of north-south direction is inadequate to explain the kinematics in the circumstellar materials around IRAS 22198+6336 probed by the blue-shifted maser features J-M.

Alternatively, distributions and proper motions of the features J-M could also be interpreted as a part of the smaller-scale expanding shell as shown in Figure 4(b), with the radius of $29.1 \pm 0.8 \text{ mas}$ ($22.2 \pm 0.6 \text{ AU}$) and the expanding velocity of $3.8 \pm 0.4 \text{ km s}^{-1}$ in the plane of the sky. In this case, the dynamical time of the expanding shell is calculated to be only 8 years. Basic characteristics of this expanding shell is quite similar to the case of Cepheus A (Torrelles et al. 2001) and W75N (Torrelles et al. 2003). Meanwhile, the nature of the possible powering source of the shell is not consistent with the position and elongation of the radio continuum emission (Sánchez-Monge et al. 2008). In addition, it is unlikely that such a shell is traced only by the most blue-shifted components. Thus, we rule out the possibility of the small-scale expanding shell as a kinematical model of the blue-shifted maser features J-M.

Brand et al. (2003) proposed three possible mechanisms to account for the velocity drift of the maser emission; a rotating circumstellar disk, acceleration/deceleration of the jets, or a precession of the jets. According to our discussion, most plausible explanation for the proper motions, radial velocity distribution, and velocity drifts of the maser features is the collimated bipolar jets along the east-west direction. Thus, the origin of the velocity shift would be the deceleration (because the radial velocity of the blue-shifted features became closer to the systemic velocity) or precession of the jets.

To distinguish between possible kinematic models, proper motion measurements of red-shifted components located at the eastern end of the maser feature distributions would be crucial. In addition, further high resolution observations of centimeter to submillimeter contin-

uum emission as well as near- and mid-infrared observations of the central YSO and collimated jets, if they are associated, would help to reveal the overall circumstellar structure of this source with accuracies of much better than $0.1''$.

5. Conclusion

In this paper, we presented the results of multi-epoch VLBI astrometry with VERA of the 22 GHz H₂O masers associated with IRAS 22198+6336 in L1204G. Using the absolute positions of total 26 maser spots that were detected in at least three observing sessions, we derived the annual parallax of IRAS 22198+6336 to be 1.309 ± 0.047 mas, corresponding to the distance of 764 ± 27 pc from the Sun. This is the most accurate distance to L1204G with the uncertainty of only 4%.

Because the newly derived distance is closer than those well adopted in the previous literatures (910 pc or 1.3 kpc), the bolometric luminosity of IRAS 22198+6336 should be significantly reduced. According to the SED of IRAS 22198+6336, the bolometric luminosity and total mass of IRAS 22198+6336 were refined to be $450L_{\odot}$ and $7M_{\odot}$, respectively. These values are not consistent with a massive YSO but are in agreement with an intermediate-mass YSO. We confirmed that IRAS 22198+6336 would be a deeply embedded intermediate-mass YSO analogous to a low-mass Class 0 source (Sánchez-Monge et al. 2008).

Together with the annual parallax, we measured the absolute proper motions of the H₂O masers. We discussed several kinematical models of the circumstellar gas such as a small scale expanding shell, collimated jets, or rotating disk. We proposed that the distributions, proper motions, and the previously reported velocity drifts (Valdettaro et al. 2002; Brand et al. 2003) of the maser features associated with IRAS 22198+6336 are consistent with the collimated bipolar jets and possibly rotating disk perpendicular to them.

IRAS 22198+6336 is one of the rare sources in the very early stage of intermediate-mass YSOs. Therefore, further high-resolution and high-sensitivity observations of the continuum emission from centimeter to submillimeter wavelength, in particular with the future interferometers such as EVLA and ALMA, and the proper motion measurements of the H₂O masers and continuum sources will be essential to reveal the kinematics and more detailed properties of IRAS 22198+6336, which will contribute to the understanding of very early stage of intermediate-mass star-formation processes.

We thank the anonymous referee for valuable comments and suggestions. We also thank Guillem Anglada and Carlos Carrasco-Gonzalez for providing us with information on the VLA observations of IRAS 22198+6336. We are grateful to the staff of all the VERA stations for their assistance in observations. TH is financially supported by Grant-in-Aids for Scientific Research from The Ministry of Education, Culture, Sports, Science and Technology (13640242, 16540224, and 20740112).

References

- Anglada, G. 1995, *Rev. Mexicana Astron. Astrof. Ser. Conf.*, 1, 67
- Brand, J., Cesaroni, R., Comoretto, G., Felli, M., Palagi, F., Palla, F., & Valdettaro, R. 2003, *A&A*, 407, 573
- Chikada, Y., et al. 1991, in *Frontiers of VLBI*, ed. H. Hirabayashi, M. Inoue, & H. Kobayashi (Tokyo: Universal Academy Press), 79
- Claussen, M. J., Marvel, K. B., Wootten, A., & Wilking, B. A. 1998, *ApJ*, 507, L79
- Crampton, D. & Fisher, W. A. 1974, *Pub. Dom. Astrophys. Obs.*, 14, 283
- Dame, T. M., et al. 1987, *ApJ*, 322, 706
- Dehnen, W. & Binney, J. J. 1998, *MNRAS*, 298, 387
- de Zeeuw, P. T., Hoogerwerf, R., de Bruijne, J. H. J., Brown, A. G. A., Blaauw, A. 1999, *AJ*, 117, 354
- Edris, K. A., Fuller, G. A., & Cohen, R. J. 2007, *A&A*, 465, 865
- Fukui, Y. 1989, in *Low-mass Star Formation and Pre-Main-Sequence Objects*, ed. B. Reipurth (Garching: ESO), 95
- Furuya, R. S., Kitamura, Y., Wootten, H. A., Claussen, M. J., Saito, M., Marvel, K. B., & Kawabe, R. 2000, *ApJ*, 542, L135
- Hachisuka, K. et al. 2006, *ApJ*, 645, 337
- Hirota, T. et al. 2007, *PASJ*, 59, 897
- Hirota, T. et al. 2008, *PASJ*, 60, 37
- Honma, M. et al. 2003, *PASJ*, 55, L57
- Honma, M. et al. 2007, *PASJ*, 59, 889
- Honma, M. et al. 2008a, submitted to *PASJ*
- Honma, M., Tamura, Y., & Reid, M. J. 2008b, *PASJ*, 60, in press
- Iguchi, S., Kurayama, T., Kawaguchi, N., Kawakami, K. 2005, *PASJ*, 57, 259
- Imai, H. et al. 2007, *PASJ*, 59, 1107
- Jenness, T., Scott, P. F., & Padman, R. 1995, *MNRAS*, 276, 1024
- Kawaguchi, N., Sasao, T., Manabe, S. 2000, in *Proc. SPIE*, 4015, *Radio Telescopes*, ed. H. R. Butcher (Washington: SPIE), 544
- Loinard, L., Mioduszewski, A. J., Rodríguez, L. F., González, R. A., Rodríguez, M. I., Torres, R. M. 2005, *ApJ*, 619, L179
- Loinard, L., Torres, R. M., Mioduszewski, A. J., Rodríguez, L. F., González-Lópezlira, R. A., Lachaume, R., Vázquez, V., & González, E. 2007, *ApJ*, 671, 546
- Loinard, L., Torres, R. M., ; Mioduszewski, A. J., & Rodríguez, L. F. 2008, *ApJ*, 675, L29
- Lombardi, M., Lada, C. J., & Alves, J. 2008, *A&A*, 480, 785
- Menten, K. M., Reid, M. J., Forbrich, J., & Brunthaler, A. 2007, *A&A*, 474, 515
- Migenes, V. et al. 1999, *ApJS*, 123, 487
- Molinari, S., Brand, J., Cesaroni, R., & Palla, F. 1996, *A&A*, 308, 573
- Moscadelli, L., Testi, L., Furuya, R. S., Goddi, C., Claussen, M., Kitamura, Y., & Wootten, A. 2006, *A&A*, 446, 985
- Palla, F., Brand, J., Cesaroni, R., Comoretto, G., & Felli, M. 1991, *A&A*, 246, 249
- Patel, N. A., Greenhill, L. J., Herrnstein, J., Zhang, Q., Moran, J. M., Ho, P. T. P., & Goldsmith, P. F. 2000, *ApJ*, 538, 268
- Perryman, M. A. C., et al. 1997, *A&A*, 323, L49
- Petrov, L., Kovalev, Y. Y., Fomalont, E., & Gordon, D. 2005, *AJ*, 129, 1163

- Reid, M. J. 1993, *ARA&A*, 31, 345
- Reid, M. J. & Brunthaler, A. 2004, *ApJ*, 616, 872
- Sánchez-Monge, Á., Palau, A., Estalella, R., Beltrán, M., & Girart, J. M. 2008, *A&A*, 485, 497
- Sandstrom, K. M., Peek, J. E. G., Bower, G. C., Bolatto, A. D., & Plambeck, R. L. 2007, *ApJ*, 667, 1161
- Sato, M. et al. 2007, *PASJ*, 59, 743
- Sato, M. et al. 2008, *PASJ*, 60, in press
- Stahler, S. W. & Palla, F. 2004, *The Formation of Stars* (Weinheim: Wiley-VCH)
- Szymczak, M., Hrynek, G., & Kus, A. J. 2000, *A&AS*, 143, 269
- Tafalla, M., Bachiller, R., & Martín-Pintado, J. 1993, *ApJ*, 403, 175
- Tofani, G., Felli, M., Taylor, G. B., & Hunter, T. R. 1995, *A&AS*, 112, 299
- Torrelles, J. M. et al. 2003, *ApJ*, 598, L115
- Torrelles, J. M. et al. 2001, *Nature*, 411, 277
- Torres, R. M., Loinard, L., Mioduszewski, A. J., & Rodríguez, L. F. 2007, *ApJ*, 671, 1813
- Ulich, B. L., Haas, R. W. 1976, *ApJS*, 30, 247
- Valdettaro, R., Palla, F., Brand, J., Cesaroni, R., Comoretto, G., Felli, M., & Palagi, F. 2002, *A&A*, 383, 244
- Wilking, B. A., Blackwell, J. H., Mundy, L. G., & Howe, J. E. 1989, *ApJ*, 345, 257
- Wouterloot, J. G. A. & Brand, J. 1989, *A&AS*, 80, 149
- Yonekura, Y., Dobashi, K., Mizuno, A., Ogawa, H., & Fukui, Y. 1997, *ApJS*, 110, 21